

Abstract

As wind farms become larger, the spacing between turbines becomes a significant design element that imposes serious economic constraints. Effects of turbine spacing on the power produced and flow structure are crucial for future development of wind energy. To investigate the turbulent flow structures in a 4×3 Cartesian wind turbine array, a wind tunnel experiment was carried out parameterizing the streamwise and spanwise wind turbine spacing. Four cases are chosen spacing turbines by 6 diameters (D) or $3D$ in the streamwise, and $3D$ or $1.5D$ in the spanwise direction. Data are obtained experimentally using stereo particle-image velocimetry. Mean streamwise velocity showed maximum values upstream of the turbine with the spacing of $6D$ and $3D$, in the streamwise and spanwise direction, respectively. Fixing the spanwise turbine spacing to $3D$, variations in the streamwise spacing influence the turbulent flow structure and the power available to following wind turbines. Quantitative comparisons are made through spatial averaging, shifting measurement data and interpolating to account for the full range between devices to obtain data independent of array spacing. The largest averaged Reynolds stress is seen in cases with spacing of $3D \times 3D$. Snapshot proper orthogonal decomposition (POD) was employed to identify the flow structures based on the turbulence kinetic energy content. The maximum turbulence kinetic energy content in the first POD mode compared with other cases is seen for turbine spacing of $6D \times 1.5D$. The flow upstream of each wind turbine converges faster than the flow downstream according to accumulation of turbulence kinetic energy by POD modes, regardless of spacing. The streamwise-averaged profile of the Reynolds stress is reconstructed using a specific number of modes for each case; the case of $6D \times 1.5D$ spacing shows the fastest reconstruction. Intermediate modes are also used to reconstruct the averaged profile and show that the intermediate scales are responsible for features seen in the original profile. The variation in streamwise and spanwise spacing leads to changes in the background structure of the turbulence, where the color map based on barycentric map and anisotropy stress tensor provides a new perspective on the nature of the perturbations within the wind turbine array. The impact of the streamwise and spanwise spacings on power produced is quantified, where the maximum production corresponds with the case of greatest turbine spacing.

6 I. INTRODUCTION

7 Allowing insufficient space between wind turbines in an array leads to decreased perfor-
8 mance through wake interaction, decreased wind velocity and an increase in the accumulated
9 fatigue loads and intermittency events on downstream turbines (Viggiano et al. 2016, Ali
10 et al. 2016a). Wind turbine wakes lead to an average loss of 10-20% of the total potential
11 power output of wind turbine array (Barthelmie et al. 2007). Extensive experimental and
12 numerical studies focus on wake properties in terms of the mean flow characteristics used to
13 obtain estimates of power production (Chamorro and Porté-Agel 2009, 2011). Wake growth
14 depends on the shape and magnitude of the velocity deficit, surface roughness, flow above
15 the canopy and spacing between the turbines.

16 Although there are many studies dealing with the effect of the density of turbines on
17 the wake recovery, it is still a debated question. The actual spacing of wind turbines can
18 vary greatly from one array to another. For example, in the Nysted farm, spacing is 10.5
19 diameters (D) downstream by $5.8D$ spanwise at the exact row (ER). The wind direction at
20 the ER is 278° and mean wind direction can slightly offset from ER by $\pm 15^\circ$ (Barthelmie
21 et al. 2010). **Of relevance, the variability in the wind direction pertains to the center of the**
22 **wake, assesses the wake width, and the character of wake behavior.** In the Horns Rev farm,
23 spacing between devices is $7D$, although aligned with the bulk flow direction spacing is as
24 much as $10.4D$. Barthelmie and Jensen (2010) showed that the spacing in the Nysted farm
25 is responsible for 68-76% of the farm efficiency variation. Hansen et al. (2012) pointed out
26 that variations in the power deficit are almost negligible when spacing is approximately $10D$
27 at the Horns Rev farm, in contrast to limited spacings that present a considerable power
28 deficit. González-Longatt et al. (2012) found that when the streamwise and spanwise spacing
29 increased, the wake coefficient, which represents the ratio of total power output with and
30 without wake effects, is increased. Further, the effect of the incoming flow direction on the
31 wake coefficient increased when the spacing of the array is reduced. Meyers and Meneveau
32 (2012) studied the optimal spacing in a fully developed wind farm under neutral stratification
33 and flat terrain. The results highlighted that, depending on the ratio of land and turbine
34 costs, the optimal spacing might be $15D$ instead of $7D$. Stevens (2015) pronounced that the
35 optimal spacing depends on the length of the wind farm in addition to the factors suggested
36 in Meyers and Meneveau (2012). Orography and wind direction are relevant when deciding

37 distance between turbines as well as layout as shown by Romanic et al. (2018). Nilsson
38 et al. (2015) performed large eddy simulations (LES) of the Lillgrund wind farm, where pre-
39 generated turbulence and wind shear are imposed in the computational domain to simulate
40 realistic atmospheric conditions. In the Lillgrund wind farm, the actual spacing is $3.3D$ and
41 $4.6D$ in the streamwise and spanwise directions. A turbine is missing near to the center of the
42 wind farm, demonstrating the effects of a farm with limited spacing and one with sufficient
43 spacing in otherwise identical operating conditions. The results of Nilsson et al. (2015) are
44 highly applicable in the current study, although their foci are on turbulence intensity effects
45 and yaw angle.

46 Further investigations in array optimization have been undertaken by changing the align-
47 ment of the wind farm, often referred to as staggered wind farms. Meyers and Meneveau
48 (2010) compared aligned versus staggered wind farms; the latter yielding a 5% increase in
49 extracted power. Yang et al. (2012) used LES to study the influence of the streamwise and
50 spanwise spacing on the power output in aligned wind farms under fully developed regime.
51 Their work confirmed that power produced by the turbines scales with streamwise spacing
52 more than with the spanwise spacing. Wu and Porté-Agel (2013) investigated turbulent flow
53 within and above aligned and staggered wind farms under neutral condition. Cumulative
54 wakes are shown to be subject to strong lateral interaction in the staggered case. In contrast,
55 lateral interaction is negligible in the aligned wind farm. Archer et al. (2013) quantified the
56 influence of wind farm layout on the power production, verifying that increasing the turbine
57 spacing in the predominant wind direction maximized the power production, regardless of
58 device arrangement in the wind farm. Stevens et al. (2016) investigated the power output
59 and wake effects in aligned and staggered wind farms with different streamwise and spanwise
60 turbine spacings. In the staggered configuration, power output in a fully developed flow de-
61 pends mainly on the spanwise and streamwise spacings, whereas in the aligned configuration,
62 power strongly depends on the streamwise spacing.

63 As wind farms become larger, the land costs and availability represent critical factors in
64 the overall value of the wind farm. Spacing between the turbines is an important design
65 factor in terms of overall wind farm performance and economic constraints. Investigation of
66 wind farms with limited spacing is important in order to quantify the effects of wind turbine
67 wake interaction on the power production. The current work compares the turbulent flow
68 in various configurations of the array, where the streamwise and spanwise spacings are var-

69 ied. The tunnel-scaled wind farm is, however, restricted to a flat surface and topographic
70 influences are not considered, although the inflow to the wind farm includes modifications
71 to more closely resemble an atmospheric boundary layer. The performance of the arrays
72 is characterized by analyzing the mean velocity, Reynolds shear stress, and power produc-
73 tion. Proper orthogonal decomposition (POD) is employed to identify coherent structures of
74 the turbulent wake associated with variations in spacing. The Reynolds stresses are recon-
75 structed from POD basis, demonstrating variation in rates of convergence according to wind
76 turbine spacing. Finally the anisotropy stress tensor is discussed to quantify the structure
77 of the stress tensor based on the invariant for the various spacings.

78 II. THEORY

79 A. Snapshot Proper Orthogonal Decomposition

80 POD is a mathematical tool that derives optimal basis functions from a set of measure-
81 ments, decomposing the flow into modes that express the most dominant features. The
82 technique, which was presented in the frame of turbulence by Lumley (1967), categorizes
83 structures within the turbulent flow depending on their energy content. Sirovich (1987)
84 presented the snapshot POD, that relaxes the computational difficulties of the classical or-
85 thogonal decomposition. POD has been used to describe coherent structures for different
86 flows, such as axisymmetric mixing layer (Glauser and George 1987), channel flow (Moin
87 and Moser 1989), atmospheric boundary layer (Shah and Bou-Zeid 2014), wake behind disk
88 (Tutkun et al. 2008), and wind turbine wake flow (Andersen et al. 2013, Bastine et al. 2014,
89 VerHulst and Meneveau 2014, Hamilton et al. 2015a, Ali et al. 2016b, 2017a).

90 The flow field, taken as the fluctuating velocity after subtracting time average mean
91 velocity from instantaneous velocity, can be represented as $u = u(\vec{x}, t^n)$, where \vec{x} and t^n
92 refer to the spatial coordinates and time at sample n , respectively. A set of the orthonormal
93 basis functions, ϕ , can be presented as

$$\phi = \sum_{n=1}^N A(t^n) u(\vec{x}, t^n), \quad (1)$$

94 where N is the number of snapshots. The largest projection can be determined using the
95 two point correlation tensor and Fredholm integral equation

$$\int_{\Omega} \frac{1}{N} \sum_{n=1}^N u(\vec{x}, t^n) u^T(\vec{x}', t^n) \phi(\vec{x}') d\vec{x}' = \lambda \phi(\vec{x}), \quad (2)$$

96 where left hand side of the equation presents a spatial correlation between two points \vec{x}
 97 and \vec{x}' , T signifies the transpose of a matrix, Ω is the physical domain, and λ are the
 98 eigenvalues. To acquire the optimal basis functions, the problem is reduced to an eigenvalue
 99 decomposition denoted as $[C][G] = \lambda[G]$, where C , G and λ are the correlation tensor, basis
 100 of eigenvectors, and eigenvalues, respectively. The matrix $[G]$ is related to the time coefficient
 101 as $[G] = [A(t^1), A(t^2), \dots, A(t^N)]^T$. The POD eigenvectors illustrate the spatial structure
 102 of the turbulent flow and the eigenvalues measure the energy associated with corresponding
 103 eigenvectors. The summation of the eigenvalues presents the total turbulent kinetic energy
 104 (E) in the flow domain. The cumulative kinetic energy fraction η and the normalized energy
 105 content of each mode ξ can be represented as $\eta_n = \sum_{j=1}^n \lambda_n / \sum_{j=1}^N \lambda_n$ and $\xi_n = \lambda_n / \sum_{j=1}^N \lambda_n$.
 106 POD is particularly useful in rebuilding the Reynolds shear stress using a limited set (N_{lm})
 107 of eigenfunctions as follows,

$$\langle u_i u_j \rangle = \sum_{n=1}^{N_{lm}} \lambda_n \phi_i^n \phi_j^n. \quad (3)$$

108 B. Anisotropy Stress Tensor

109 Turbulence is often described through the Reynolds stress tensor. Rotta (1951) developed
 110 the Reynolds stress anisotropy tensor, as $a_{ij} = \overline{u_i u_j} - \frac{2}{3} k \delta_{ij}$, where δ_{ij} is the Kronecker delta
 111 and k represents the turbulence kinetic energy and is defined by $k = 0.5 \sum_{i=1}^3 \langle u_i u_i \rangle$. The
 112 deviatoric tensor is obtained, $b_{ij} = \overline{u_i u_j} / \overline{u_k u_k} - \frac{1}{3} \delta_{ij}$. The second and third scalar invariants
 113 are defined as $6\eta^2 = b_{ij} b_{ji}$ and $6\xi^3 = b_{ij} b_{jk} b_{ki}$, respectively (see Pope (2000), Lumley and
 114 Newman (1977) for more details). The second invariant, η , measures the degree of the
 115 anisotropy and the third invariant, ξ , specifies the state of turbulence. Alternatively, the
 116 eigenvalue decomposition of the normalized Reynolds stress anisotropy tensor can be used to
 117 derive the the second and third invariants as $\eta^2 = \frac{1}{3} (\lambda_1^2 + \lambda_1 \lambda_2 + \lambda_2^2)$ and $\xi^3 = -\frac{1}{2} \lambda_1 \lambda_2 (\lambda_1 + \lambda_2)$.
 118 In an attempt to further facilitate the study of turbulence anisotropy, Banerjee et al. (2007)
 119 presented a linearized anisotropy tensor invariants, termed barycentric map (BM) as follows,

TABLE I: Summary of the special turbulence cases described by the barycentric map.

Cases	Eigenvalues
Three-component	$\lambda_1 = \lambda_2 = \lambda_3 = 0$
Two-component	$\lambda_1 = \lambda_2 = \frac{1}{6}, \lambda_3 = -\frac{1}{3}$
One-component	$\lambda_1 = \frac{2}{3}, \lambda_2 = \lambda_3 = -\frac{1}{3}$

$$\hat{b}_{ij} = C_{1c} \begin{pmatrix} 2/3 & 0 & 0 \\ 0 & -1/3 & 0 \\ 0 & 0 & -1/3 \end{pmatrix} + C_{2c} \begin{pmatrix} 1/6 & 0 & 0 \\ 0 & 1/6 & 0 \\ 0 & 0 & -1/3 \end{pmatrix} + C_{3c} \begin{pmatrix} 0 & 0 & 0 \\ 0 & 0 & 0 \\ 0 & 0 & 0 \end{pmatrix}, \quad (4)$$

120 where C_{1c} , C_{2c} and C_{3c} are the coefficients that represent the boundary of the barycentric
 121 map. The BM coefficients are determined as $C_{1c} = \lambda_1 - \lambda_2$, $C_{2c} = 2(\lambda_2 - \lambda_3)$, and $C_{3c} =$
 122 $3\lambda_3 + 1$. The three basis matrices in equation (4) represent the three vertices of the equilateral
 123 triangle, with the following coordinates (x_{1c}, y_{1c}) , (x_{2c}, y_{2c}) and (x_{3c}, y_{3c}) . Table I presents
 124 the three turbulence states corresponding with the vertices of the BM, which also correspond
 125 to either isotropic (three-component), one- or two-component turbulence. As a result, any
 126 realizable turbulence state can be represented as follows,

$$x_{new} = C_{1c}x_{1c} + C_{2c}x_{2c} + C_{3c}x_{3c}, \quad (5)$$

$$y_{new} = C_{1c}y_{1c} + C_{2c}y_{2c} + C_{3c}y_{3c}. \quad (6)$$

127 Emory and Iaccarino (2014) also introduced a color map based visualization technique that
 128 aids to interpret the spatial distribution of the normalized anisotropy tensor. In this case,
 129 they attributed to each vertex of the barycentric map an RGB (Red-Green-Blue) color, see
 130 figure 1 for more details. This color map technique combines the coefficients C_{1c} , C_{2c} and
 131 C_{3c} to generate an RGB map such that,

$$\begin{bmatrix} R \\ G \\ B \end{bmatrix} = C_{1c}^* \begin{bmatrix} 1 \\ 0 \\ 0 \end{bmatrix} + C_{2c}^* \begin{bmatrix} 0 \\ 1 \\ 0 \end{bmatrix} + C_{3c}^* \begin{bmatrix} 0 \\ 0 \\ 1 \end{bmatrix}. \quad (7)$$

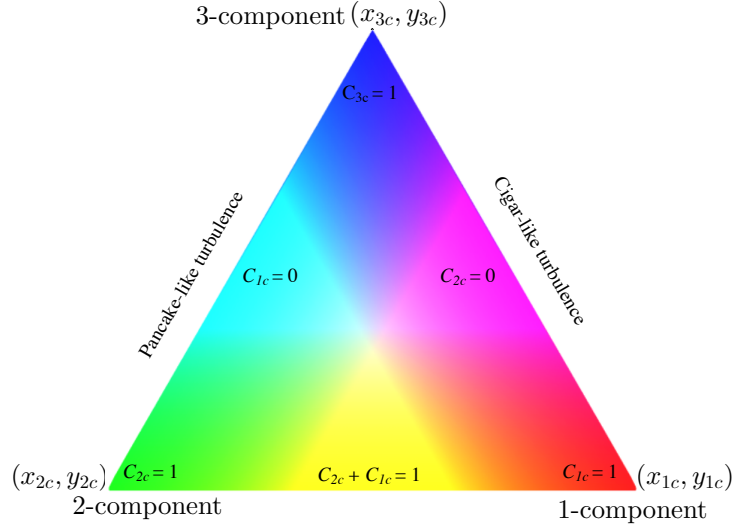


FIG. 1: Schematic representation of the Barycentric map (BM) with color map.

132 where C_{ic}^* are the modified coefficients that can be determined as $C_{ic}^* = (C_{ic} + 0.65)^5$. The
 133 coefficient with value of (0.65 and 5) is applied as it provides the optimal visualization; other
 134 coefficients are tested with less success in terms of marking differences. As a result, one-
 135 component turbulence is associated to the red color, two-component turbulence to green,
 136 and three-component (isotropic turbulence) to blue, see figure 1. The anisotropy has been
 137 examined in different types of flow, including pipe and duct flows (Antonia et al. 1991,
 138 Krogstad and Torbergsen 2000), atmospheric boundary layer (Klipp 2010, 2012) as well as
 139 the wake of a wind turbine (Gómez-Elvira et al. 2005, Hamilton and Cal 2015, Ali et al.
 140 2017b,c). Here we will used the anisotropy stress tensor is employed to quantify the effect
 141 of the spacing on the turbulence states.

142 III. EXPERIMENTAL DESIGN

143 A 4×3 array of wind turbines is placed in the closed-circuit wind tunnel at Portland
 144 State University to study the effects due to variation in streamwise and spanwise spacing in
 145 a wind turbine array. The dimensions of the wind tunnel test section are 5 m (long), 1.2 m
 146 (wide) and 0.8 m (high). **The blockage ratio is less than 5% in the test section.** The entrance
 147 of the test section is conditioned by the passive grid, which consists of 7 horizontal and 6
 148 vertical rods, to introduce large-scale turbulence. Nine vertical acrylic strakes, located at

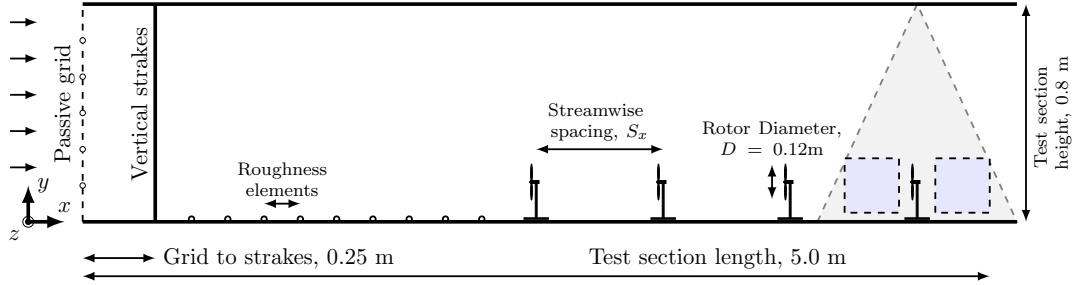


FIG. 2: Experimental Setup. Dashed gray lines indicate the placement of the laser sheet relative to the model wind turbine array. Filled gray boxes indicate measurement locations discussed below.

149 0.25 m downstream of the passive grid and 2.15 m upstream of the first row of the wind
 150 turbine, are used to modify the inflow. The thickness of the strakes is 0.0125 m and are
 151 spaced every 0.136 m across the test section. Surface roughness was introduced to the wall
 152 as a series of chains with a diameter of 0.0075 m, spaced 0.11 m apart. Figure 2 shows the
 153 schematic of the experimental setup.

154 Sheet steel of 0.0005 m thick is used to construct the 3-bladed wind turbine rotors.
 155 The diameter of the rotor is $D = 0.12$ m, equal to the height of the turbine tower. The
 156 scaled turbine models are manufactured in-house. Based on full scale turbines with a 100
 157 m rotor diameter and a 100 m hub height, the scaled models are at 1:830 scale. **In this**
 158 **study, the Reynolds number in the entrance row turbines is approximately the same order**
 159 **of magnitude of the independent range detailed in Chamorro et al. (2012).** The rotor blades
 160 are steel sheets laser cut to shape and are 0.0005 m thick. The blades are shaped using a die
 161 press. The die press is designed in-house to produce a 15 degree pitch from the plane of the
 162 rotor and a 10 degree twist at the tip. Figure 3 presents the schematic of the wind turbine
 163 model. **The wind turbine model design used is that presented in Cal et al. (2010), Kang and**
 164 **Meneveau (2010) and Hamilton et al. (2015b).** Operating conditions for the wind turbines
 165 are also scaled, namely the power coefficient, C_p and tip-speed ratio, λ , which are detailed
 166 in Hamilton et al. (2015b) The streamwise integral length scale is approximately 0.13 m,
 167 which is the same order of magnitude as the turbine rotor and representative of conditions
 168 seen by full-scale turbines in atmospheric flows. A DC electrical motor of 0.0013 m diameter
 169 and 0.0312 m long formed the nacelle of the turbine and is aligned with the flow direction.
 170 A torque-sensing system is connected to the DC motor shaft following the design outlined
 171 in Kang and Meneveau (2010). The torque sensor consists of a strain gauge, Wheatstone

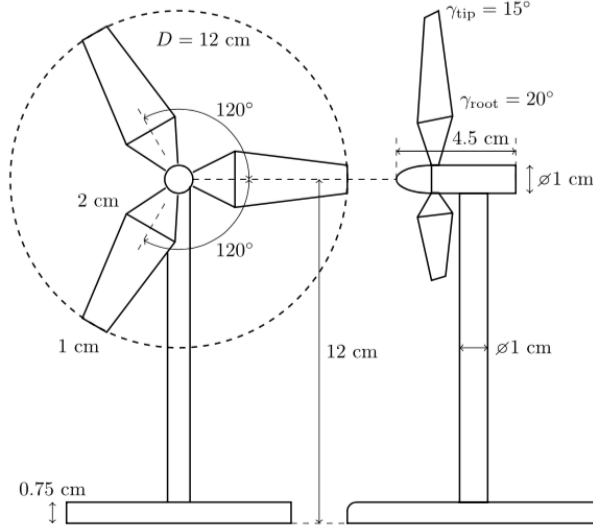


FIG. 3: Schematic representation of the wind turbine model (Hamilton and Cal 2015).

172 bridge and the Data Acquisition with measuring software to collect the data.

173 The flow field is sampled in four configurations of a model-scale wind turbine array,
 174 classified as $C_{S_x \times S_z}$, shown in Table II. Permutations of the streamwise spacing (S_x) of $6D$
 175 and $3D$ and spanwise spacing (S_z) of $3D$ and $1.5D$ are examined. Stereoscopic particle image
 176 velocimetry (SPIV) is used to measure streamwise, wall-normal and spanwise instantaneous
 177 velocity at the upstream and downstream of the wind turbine at the center line of the
 178 fourth row as shown in figure 4. At each measurement location, 2000 images are taken,
 179 to ensure convergence of second-order statistics. **The sampling rate of the SPIV system is**
 180 **fixed at 5 Hz.** SPIV equipment is LaVision and consists of a Nd:Yag (532nm, 1200mJ, 4ns
 181 duration) double-pulsed laser and four 4 MP ImagerProX CCD cameras positioned for the
 182 upstream and downstream of the wind turbine. Neutrally buoyant fluid particles of diethyl
 183 hexyl sebacate are introduced to the flow and allowed to mix. Consistent seeding density is
 184 maintained in order to mitigate measurement errors. The laser sheet is approximately 0.001
 185 m thick with less than 5 mrad divergence angle. Each measurement window is $0.2 \text{ m} \times 0.2$
 186 m aligned with the center of each turbine, parallel to the bulk flow. A multi-pass fast Fourier
 187 transformation is used to process the raw data into vector fields. Erroneous measurement
 188 of the vector fields are replaced using Gaussian interpolation of neighboring vectors. **Based**
 189 **on the variability estimator (George 2013), the error of the SPIV measurements is on the**
 190 **order of 3%. The major uncertainty pertaining to the out-of-plane (spanwise) component.**

TABLE II: Streamwise and spanwise spacing of the experimental tests.

Cases	S_x	S_z	Occupied Area
$C_{6 \times 3}$	$6D$	$3D$	$18D^2$
$C_{3 \times 3}$	$3D$	$3D$	$9D^2$
$C_{3 \times 1.5}$	$3D$	$1.5D$	$4.5D^2$
$C_{6 \times 1.5}$	$6D$	$1.5D$	$9D^2$

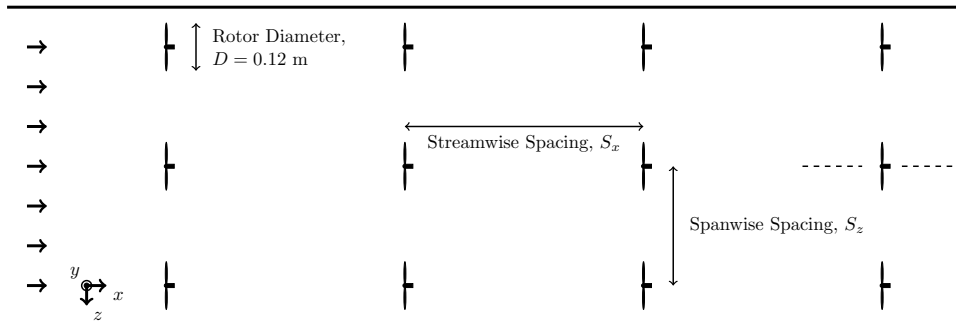


FIG. 4: Top view of 4 by 3 wind turbine array. The dash lines at the last row centerline turbine represent the measurement locations.

191 IV. RESULTS

192 A. Statistical Analysis.

193 Characterization of the wind turbine wake flow is presented by the streamwise mean
 194 velocity and Reynolds shear stress, with the aim to understand the influence of turbine-
 195 to-turbine spacing. Figure 5 presents the streamwise normalized mean velocity, U/U_∞ ,
 196 upstream and downstream of each wind turbine for the cases $C_{6 \times 3}$, $C_{3 \times 3}$, $C_{3 \times 1.5}$ and $C_{6 \times 1.5}$.
 197 The inflow mean velocity at the hub height U_∞ is used in the normalization, where $U_\infty =$
 198 5.5 m s^{-1} . The left and right contour plots of each case present the flow upstream and
 199 downstream of each turbine, respectively. At upstream measurement window, case $C_{6 \times 3}$
 200 exhibits the largest streamwise mean velocities due to greater recovery of the flow upstream
 201 of the turbine. Although the streamwise spacing of case $C_{6 \times 1.5}$ is similar that of case $C_{6 \times 3}$,
 202 the former shows reduced hub height velocity. The normalized mean velocity is about 0.567
 203 compared with 0.66 in case $C_{6 \times 3}$, confirming the influence of the spanwise spacing on wake
 204 evolution and flow recovery. Variations perceived between case $C_{3 \times 3}$ and $C_{3 \times 1.5}$ are small,

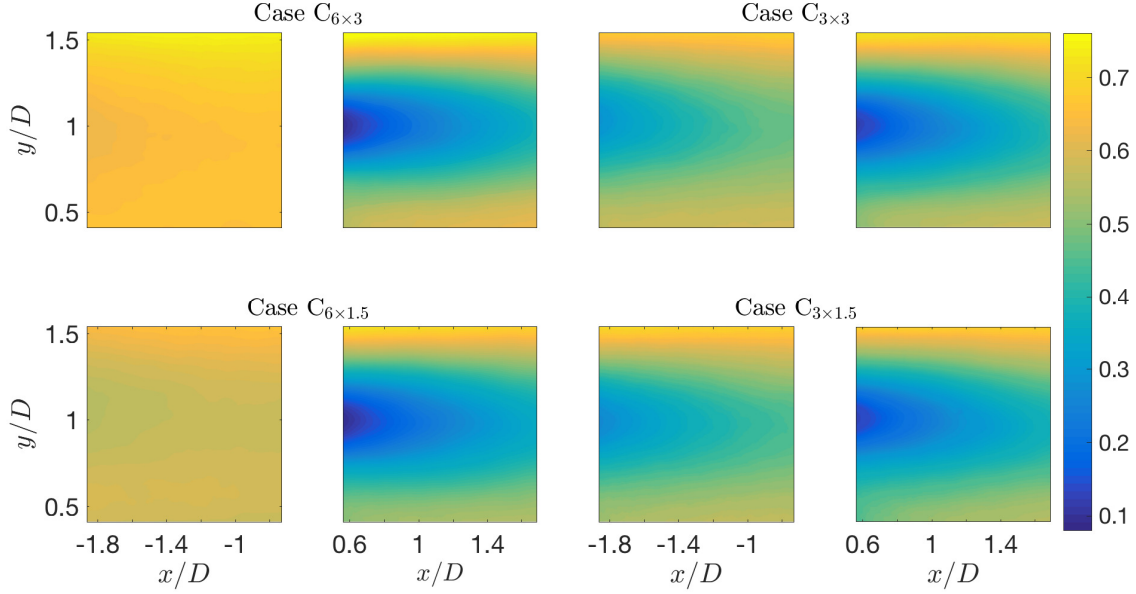


FIG. 5: Normalized streamwise velocity, U/U_∞ , at upstream and downstream of the cases $C_{6 \times 3}$, $C_{3 \times 3}$, $C_{3 \times 1.5}$, and $C_{6 \times 1.5}$.

205 where case $C_{3 \times 3}$ demonstrates higher velocities by approximately 2%. Downstream of the
 206 turbine, the four cases show more relevant differences especially above the top tip and below
 207 the bottom tip, where case $C_{6 \times 3}$, once again, shows the greatest velocities by approximately
 208 20%. Case $C_{3 \times 3}$ also shows higher velocities below the bottom tip compared with cases
 209 $C_{3 \times 1.5}$ and $C_{6 \times 1.5}$. The normalized mean streamwise velocity and the turbulence intensity in
 210 Nilsson et al. (2015) showed similar compound wakes from the upstream and downstream
 211 turbines and confirmed the current result of cases $C_{3 \times 3}$ and $C_{3 \times 1.5}$. In that study, there was
 212 one location with an absent turbine and the flow was given extra space for recovery. The
 213 recovered wake flow in Nilsson et al. (2015) is similar to the present cases $C_{6 \times 3}$ and $C_{6 \times 1.5}$.

214 Figure 6 compares the in-plane normalized Reynolds shear stress $-\overline{uv}/U_\infty^2$ for all test
 215 cases. The fluctuating velocities in streamwise and wall-normal direction are denoted as u
 216 and v , respectively. In the upstream window, cases $C_{3 \times 3}$ and $C_{3 \times 1.5}$ display higher stress
 217 compared with $C_{6 \times 3}$ and $C_{6 \times 1.5}$. Although the spanwise spacing of case $C_{3 \times 1.5}$ is half of
 218 case $C_{3 \times 3}$, no relevant differences are apparent. In the downstream window, comparison
 219 indicates that reducing streamwise spacing increases the Reynolds shear stress. The average
 220 value of the shear stress in the wake is 16% greater for $C_{3 \times 3}$ than for $C_{6 \times 3}$. A similar effect is
 221 observed in case $C_{3 \times 1.5}$, where average value of the stress is 2% greater than that of $C_{6 \times 1.5}$.

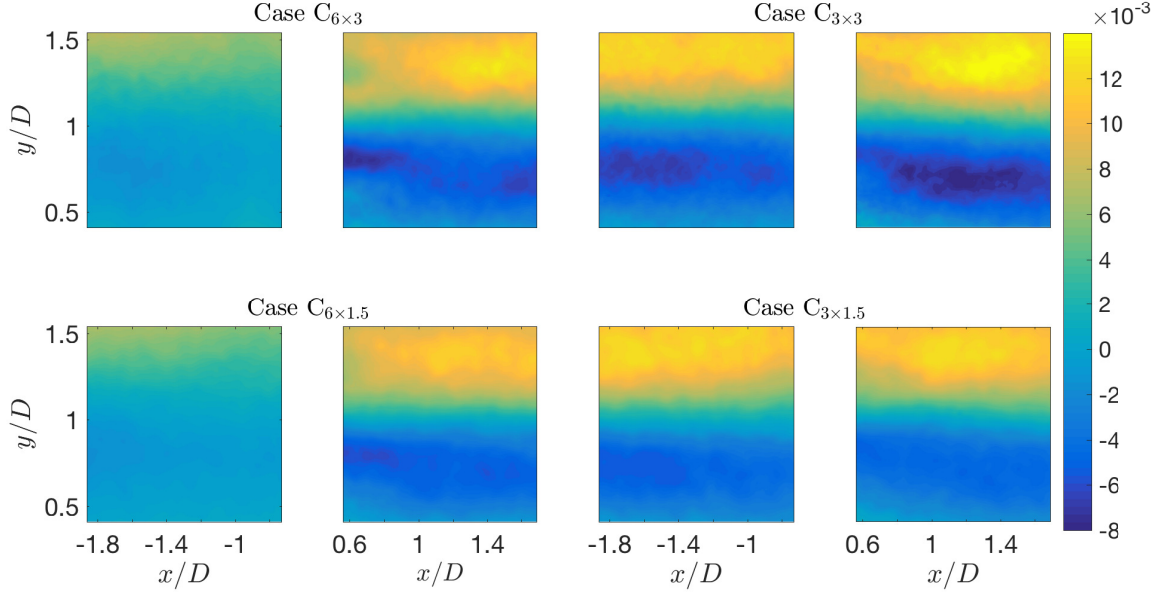


FIG. 6: Normalized Reynolds shear stress, $-\overline{uv}/U_\infty^2$, in upstream and downstream of the each measurement case.

222 The effect of spanwise spacing is more pronounced when the streamwise spacing is $3D$; the
 223 average shear stress is approximately 20% greater in $C_{3 \times 1.5}$ than in $C_{3 \times 3}$.

224 B. Averaged Profiles.

225 Spatial averaging of the flow statistics is undertaken by moving the upstream domain
 226 of each case beyond its corresponding downstream domain and performing streamwise av-
 227 eraging, following the procedure in Cal et al. (2010). Though the spatial averaging, it is
 228 possible to compare key data from different cases taking into account the different streamwise
 229 spacings. Streamwise averaging is denoted by $\langle \cdot \rangle_x$. Figure 7(a) shows profiles of streamwise-
 230 averaged mean velocity for all four cases. Cases $C_{6 \times 3}$ and $C_{3 \times 1.5}$ show the largest and
 231 smallest velocity deficits, respectively. At hub height, the velocity of the case $C_{6 \times 3}$ is ap-
 232 proximately 2.25 m s^{-1} whereas case $C_{3 \times 1.5}$ shows a velocity of approximately 1.6 m s^{-1} .
 233 Comparing to $C_{6 \times 3}$, the change seen in the spatially-averaged velocity is greater in $C_{3 \times 3}$
 234 than in $C_{6 \times 1.5}$, confirming that the impact of reducing streamwise spacing is greater than
 235 changing the spanwise spacing. **Interestingly, a reduction in streamwise spacing shows less**
 236 **effect when the spanwise spacing $S_z = 1.5D$. This is a result due to constraining the wake**

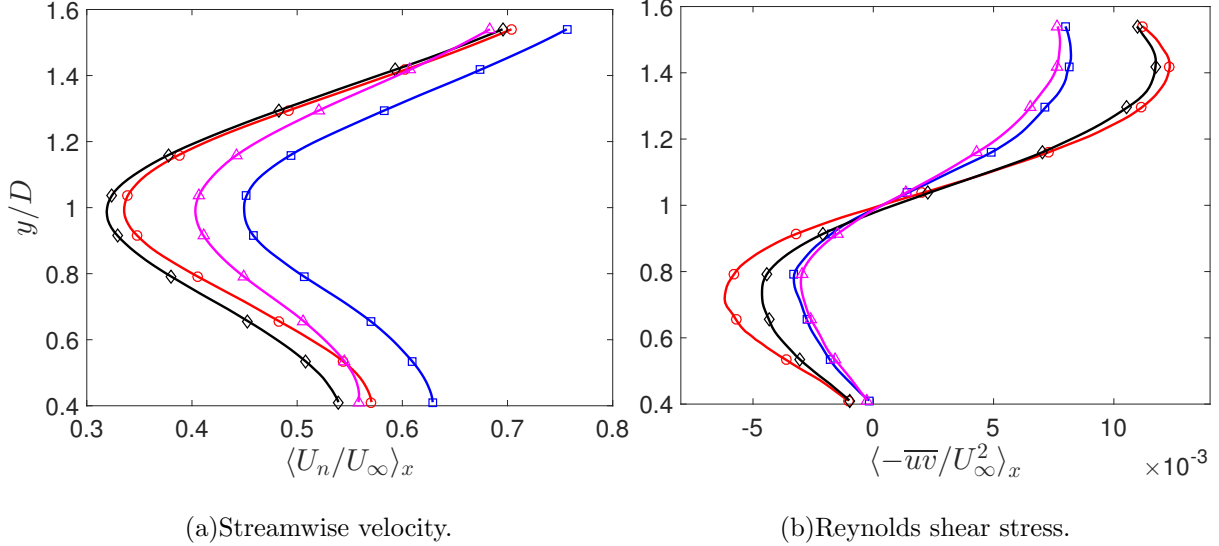


FIG. 7: Streamwise-averaged profiles of streamwise velocity, and Reynolds shear stress for four different cases $C_{6 \times 3}$ (\square), $C_{3 \times 3}$ (\circ), $C_{3 \times 1.5}$ (\diamond), and $C_{6 \times 1.5}$ (\triangle).

237 as it interacts with wakes from the other various turbines thus suppressing the development
 238 in the streamwise and spanwise direction. Therefore, a reduction in the spanwise turbine-
 239 to-turbine distance increases the lateral interactions.

240 Figure 7(b) contains the streamwise-averaged Reynolds shear stress $\langle -\overline{uv}/U_\infty^2 \rangle_x$ for cases
 241 $C_{6 \times 3}$ through $C_{6 \times 1.5}$. Slightly decreased in $\langle -\overline{uv}/U_\infty^2 \rangle_x$ are attained in case $C_{6 \times 1.5}$, where the
 242 spanwise spacing is reduced. Reducing spanwise spacing shows an important influence when
 243 the streamwise spacing is $x/D = 3$. The streamwise spacing plays a larger role than the
 244 spanwise spacing, *i.e.* the maximum differences between the Reynolds shear stress profiles
 245 are detected between cases $C_{6 \times 3}$ and $C_{3 \times 3}$. Interestingly, the largest difference between the
 246 spatially-averaged Reynolds shear stress is found between cases $C_{6 \times 3}$ and $C_{3 \times 3}$, located at
 247 $y/D \approx 0.7$ and $y/D \approx 1.4$. Furthermore, the four cases have approximately zero Reynolds
 248 shear stress at the inflection point located at hub height. In addition, case $C_{3 \times 3}$ displays
 249 the maximum Reynolds stress and case $C_{6 \times 1.5}$ presents the minimum stress.

250 C. Proper Orthogonal Decomposition.

251 Based on the velocity field, the spatially integrated turbulent kinetic energy is expressed
 252 by the eigenvalue of each POD mode. The normalized cumulative energy fraction η_n for
 253 upstream and downstream measurement windows are presented in figure 8(a) and (b), re-

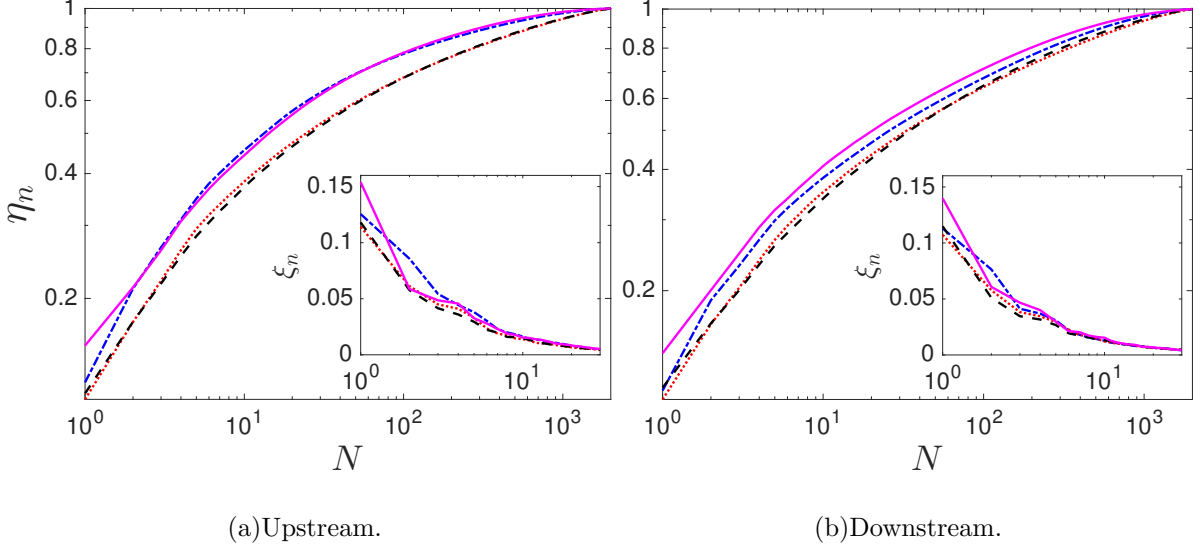


FIG. 8: Energy content of the POD modes for four different cases: $C_{6 \times 3}$ ($-\cdot-$), $C_{3 \times 3}$ ($\cdot\cdot\cdot$), $C_{3 \times 1.5}$ ($---$), and $C_{6 \times 1.5}$ ($-$).

254 spectively. Inset figures exhibit the normalized energy content per mode, ξ_n . Upstream of
 255 the turbine, cases $C_{6 \times 3}$ and $C_{6 \times 1.5}$ converge faster than cases $C_{3 \times 3}$ and $C_{3 \times 1.5}$, respectively.
 256 These results are attributed to the reduction on the streamwise spacing. The convergence
 257 of case $C_{3 \times 3}$ is approximately coincident with case $C_{3 \times 1.5}$. For the downstream flow, case
 258 $C_{6 \times 1.5}$ converges faster than the other cases, thereafter it is ordered as $C_{6 \times 3}$, $C_{3 \times 3}$ and $C_{3 \times 1.5}$
 259 in succession. The comparison between the upstream and downstream windows reveals that
 260 energy accumulates in fewer modes upstream in each case, *e.g.*, case $C_{6 \times 3}$ requires 14 modes
 261 to obtain 50% of the total kinetic energy in the upstream window, whereas 26 modes are
 262 required to obtain the same percentage of energy downstream of the turbine. Cases $C_{6 \times 1.5}$
 263 and $C_{3 \times 1.5}$ show the maximum and minimum variations in λ_1 , respectively. This observation
 264 can be attributed to the structure of the upstream flow of case $C_{6 \times 1.5}$, which is rather recov-
 265 ered, compared to the downstream flow, where the turbulence is high in energy content and
 266 more complex. However, the upstream and downstream windows of case $C_{3 \times 1.5}$ are more
 267 similar in terms of turbulence and organization. From mode 2 through 10, the starkest dif-
 268 ference between the upstream and downstream is found in case $C_{6 \times 3}$. Increasing the spacing
 269 area per turbine provides room for the flow to become more homogeneous in the upstream
 270 window and exhibit the most significant momentum deficit in the wake, accounting for the
 271 differences seen in η_n upstream and downstream.

272 The streamwise component of several POD modes is shown for all cases in figures 9

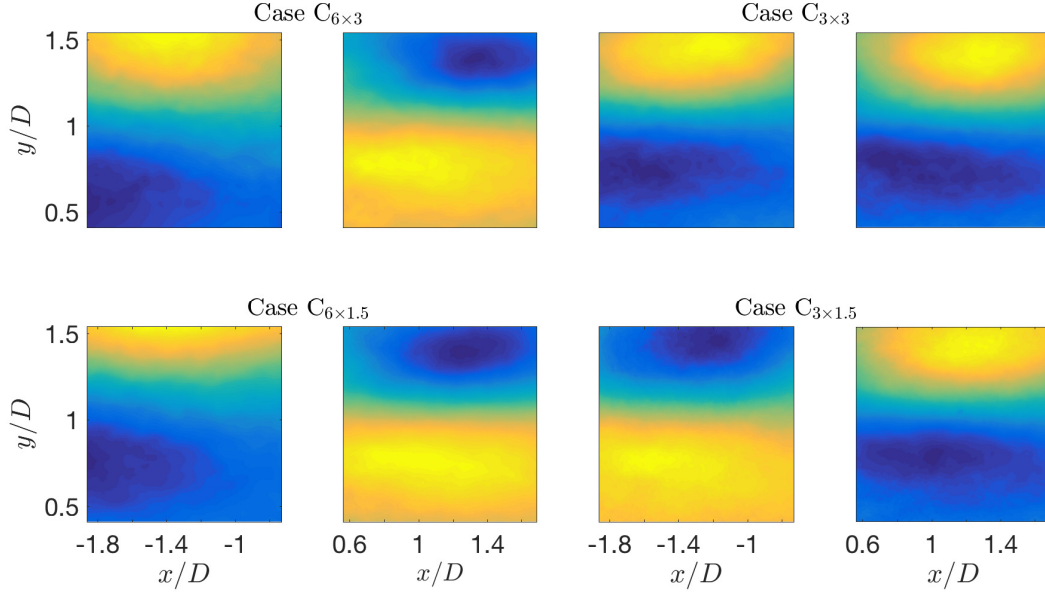


FIG. 9: The first mode upstream and downstream of the each case.

273 through 11. These modes are selected because they provide a range of large and intermedi-
 274 ate scales, and highlight the discrepancies among the cases. Figure 9 presents the first POD
 275 mode at the upstream and downstream of the considered cases. The four cases show small
 276 gradients in the streamwise direction compared to a large gradient in the wall-normal direc-
 277 tion. Although the four cases show a divergence between the eigenvalues of the first mode,
 278 the eigenfunctions display very similar structures. For case $C_{6 \times 3}$ energy of the first POD
 279 mode shows decreases by 1.25% comparing the upstream eigenvalue to the downstream one,
 280 see figure 8. Smaller variations of 0.68% and 0.32% are observed in the cases $C_{3 \times 3}$ and $C_{3 \times 1.5}$,
 281 respectively. Consequently, the structures of upstream and downstream of these cases are
 282 approximately equivalent. The similarity in the shape of the structure is observed between
 283 cases $C_{6 \times 3}$ and $C_{6 \times 1.5}$ despite the turbulence kinetic energy difference between them being
 284 about 3%. The upstream of cases $C_{6 \times 3}$ and $C_{6 \times 1.5}$ is representative of the recovering part of
 285 the flow, in contrast to the downstream that presents the wake region. This difference in the
 286 physical space has an impact in the low number POD modes that show the discrepancy in
 287 the coherent structures between the upstream and downstream. In the $C_{3 \times 3}$ arrangement,
 288 upstream and downstream both contain similar behaviors, thus pointing to the resemblance
 289 in the structure. Alike observations can be extracted from case $C_{3 \times 1.5}$. Of note, a difference
 290 in sign of the eigenvectors is present, which is one of the POD properties.

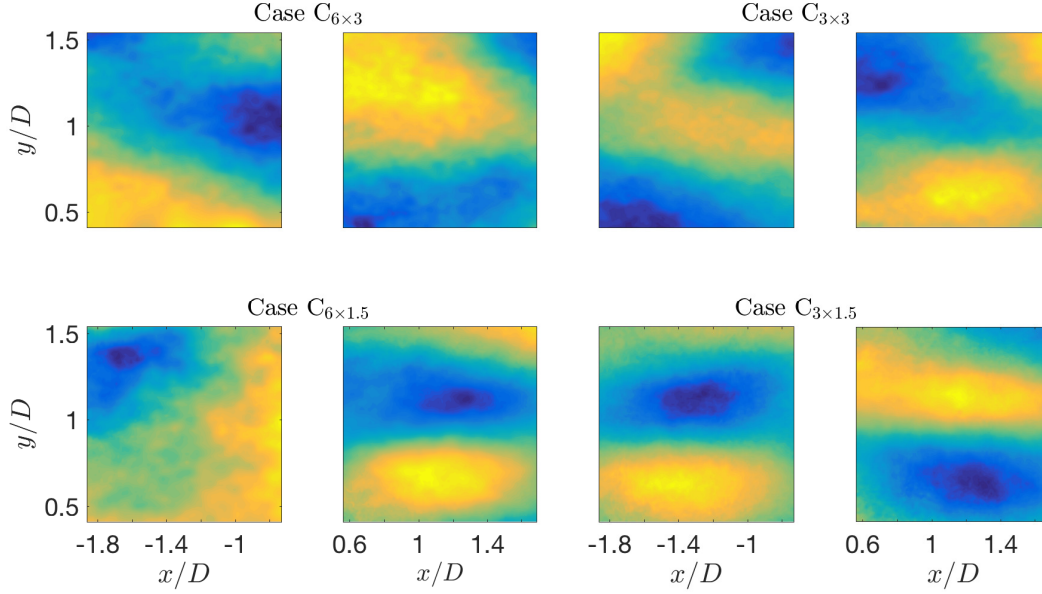


FIG. 10: The fifth mode upstream and downstream of the each case.

291 Figure 10 presents the fifth POD mode of the four cases that show a combination of POD
 292 and Fourier (homogenous) modes in the streamwise direction. Although the fifth mode of the
 293 four cases contains $\approx 74\%$ less energy of than the first mode, large scales are still pronounced.
 294 Smaller features also appear in the upstream and the downstream windows. The upstream
 295 window of cases $C_{6 \times 3}$, $C_{3 \times 3}$, and $C_{3 \times 1.5}$ is shifted horizontally in the downstream window.
 296 The upstream and downstream widows of case $C_{3 \times 1.5}$ look like the first mode, but at a
 297 reduced scale. The same trend is observed in the downstream window of the case $C_{6 \times 1.5}$.

298 Figure 11 presents the twentieth POD mode, where small structures become noticeable
 299 in both upstream and downstream windows. The upstream measurement window of cases
 300 $C_{6 \times 3}$ and $C_{6 \times 1.5}$ shows large scale structures compared with the other two cases. Although,
 301 after mode 10, there is no significant difference in the energy content from case to case, the
 302 structure of the modes shows a significant discrepancy between the cases confirming that
 303 the intermediate modes are associated with the inflow characterizations.

304 D. Reconstruction of Averaged Profile.

305 Combining the POD modes with the corresponding time coefficient gives these modes the
 306 physical interpretation and shows the contribution of these modes in the flow perturbation.

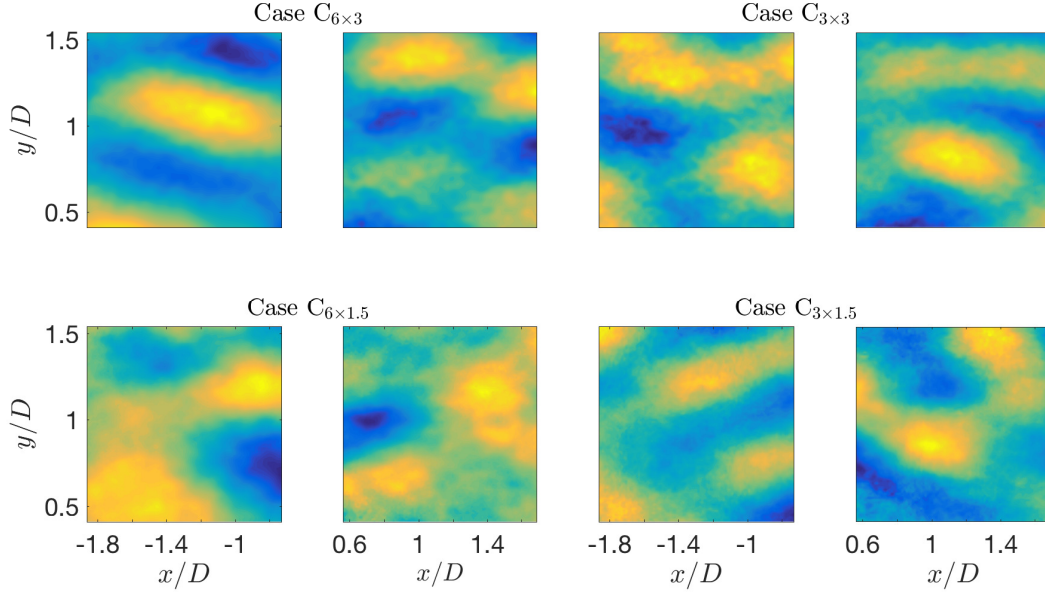


FIG. 11: The twentieth mode upstream and downstream of the each case.

307 A reduced degree of the turbulence kinetic energy is considered using only a few modes
 308 to reconstruct the streamwise-averaged profiles of Reynolds shear stress. Reconstructions
 309 are made using either the first mode, the first 5, 10, 25, or 50 modes to represent the
 310 stress as shown in figure 12. Inset figures present the Reynolds shear stress construction
 311 using the modes 5-10, 5-25, and 5-50, respectively, excluding the first four modes isolates
 312 contributions from intermediate modes. The black lines are the streamwise average of full
 313 data from figure 7(b). Using an equal number of modes, case $C_{6 \times 1.5}$ rebuilds the profiles
 314 of the Reynolds shear stress faster than the other cases. Case $C_{6 \times 3}$ also shows the fast
 315 reconstruction and the dissimilarity with case $C_{6 \times 1.5}$ is mainly in the profile of first mode
 316 (red line) and the first five modes (blue line). Cases $C_{3 \times 3}$ and $C_{3 \times 1.5}$ show approximately
 317 the same trends in reconstruction profiles. Below hub height, the four cases show the same
 318 trend of the first mode profiles, where the contribution in the reconstruction profiles is zero.
 319 The first five modes display exactly the form of the full data profile of individual case. The
 320 maximum difference between the successive reconstruction profiles occurs between the first
 321 mode and the first five modes. The cases $C_{6 \times 3}$, $C_{3 \times 3}$ and $C_{3 \times 1.5}$ show moderate variation
 322 between the profiles of the reconstructed stress resulting from first five and first ten modes
 323 (red and green lines, respectively). After mode 10 contributions by each additional mode
 324 are quite small, shown by pink and gray lines.

325 The maximum difference between the full data and the reconstructed profiles is located
 326 at $y/D \approx 0.75$ and $y/D \approx 1.4$, where the extrema in $\langle -\overline{uv} \rangle_x$ are located. Generally, faster
 327 reconstruction implies that the flow possesses coherent structures with a greater portion of
 328 the total kinetic energy. Consequently, the flow characterized with greater coherence in the
 329 cases $C_{6 \times 3}$ and $C_{6 \times 1.5}$. In cases C_{33} and $C_{31.5}$, less energetic features are observed due to the
 330 reduced spacing effect that leads to a reduction of the mean velocities within the canopy and
 331 an increase in lateral wake interactions. These interactions, which become larger as a result
 332 of the accumulated wakes, expand downstream of the rotor. Thus, the streamwise spacing
 333 allows for the flow to recover and therefore produce larger, more coherent structures within
 334 the domain, which in comparison eclipses variations produced by the spanwise spacing. Also,
 335 the large spacing offers a larger frontal area to the wind coming from above the lateral sides.

336 To quantify the contribution of the moderate-scaled structures, Reynolds shear stress is
 337 reconstructed using the intermediate modes. As can be shown in the insets of figure 12,
 338 the full data profile (black line) is compared with profiles reconstructed from modes 5-10
 339 (red line), 5-25 (blue line), and 5-50 (green lines). The intermediate modes in each case
 340 approximately take the form of the full data profiles below the hub height, although the
 341 magnitudes of the reconstructions are smaller than those of the full data statistics. Recon-
 342 struction Reynolds shear stress in cases $C_{6 \times 3}$ and $C_{3 \times 1.5}$ show minute variations between
 343 the successive reconstruction profiles and are essentially vertical lines above the hub height.
 344 This trend is opposite to the trend that is shown in the first mode profile. Cases $C_{3 \times 3}$ and
 345 $C_{3 \times 1.5}$ show a difference between the successive profiles above the hub height. The maximum
 346 difference is observed between the reconstructed profiles from modes 5-10 and from 5-25 due
 347 to the turbulence kinetic energy contained within these modes.

348 E. Anisotropy Stress Tensor

349 To examine the dynamics and energy transfer in the wind turbine arrays with different
 350 streamwise and spanwise spacings, a description of the anisotropy in the upstream and
 351 downstream of the wind turbines is presented in figure 13. A visualization of the turbulence
 352 state is obtained via the color map representing the barycentric map as described in section
 353 II B, where it efficiently distinguishes among the cases in terms of wake propagation and wake
 354 interaction. The variation in the spacings changes the background turbulence structure.

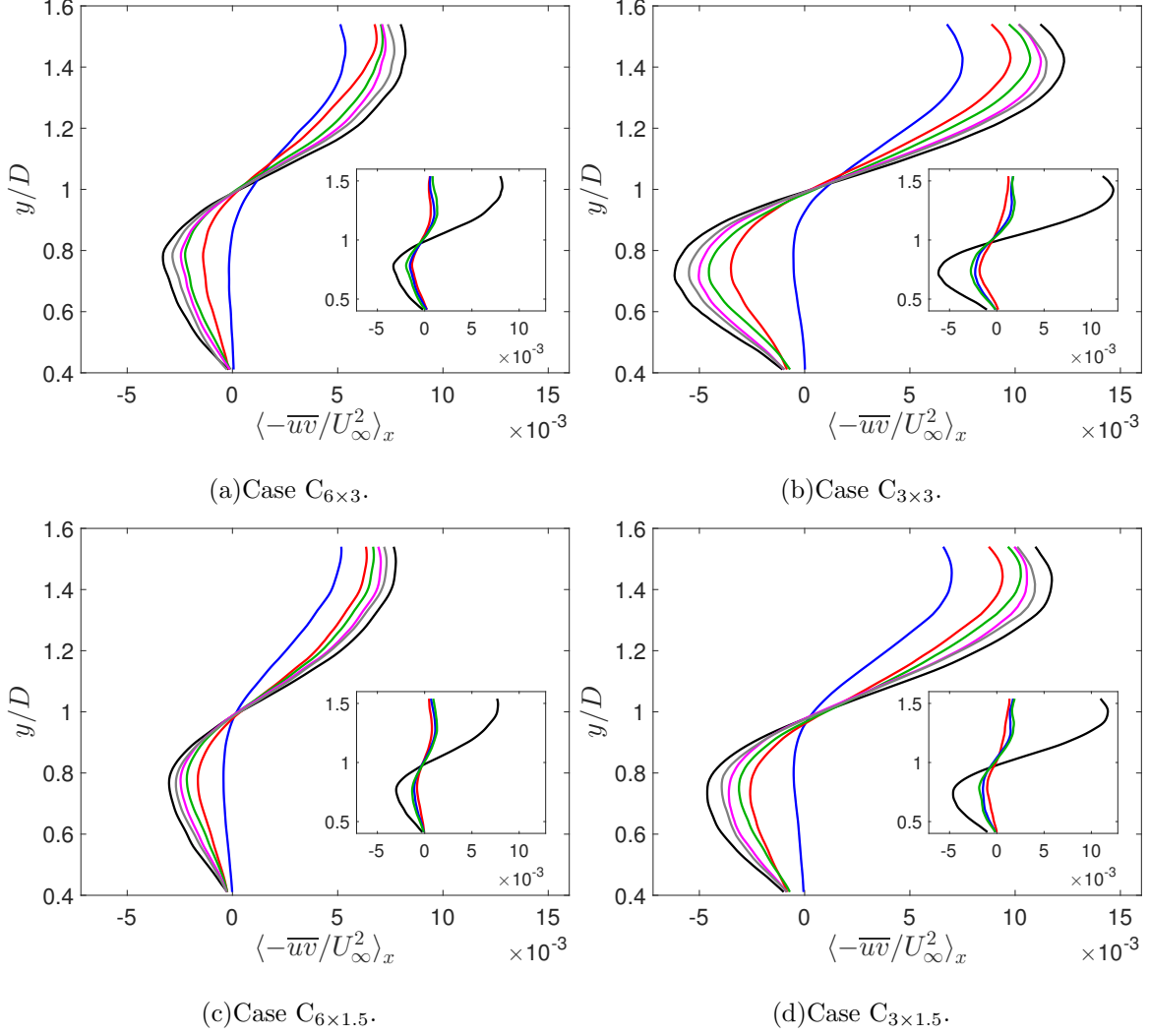


FIG. 12: Reconstruction Reynolds shear stress using: first mode (—), first 5 modes (—), first 10 modes (—), first 25 modes (—) and first 50 modes (—). Full data statistics (—). The insets show the reconstruction using modes 5-10 (—), 5-25 (—), and 5-50 (—).

355 The upstream of cases $C_{6 \times 3}$ and $C_{6 \times 1.5}$ shows the turbulence state close to the isotropy limit
 356 especially in hub height region as a result of the wake recovery occurring under a relatively
 357 long spacing distance. Below the bottom tip, these cases show pancake-like turbulence due to
 358 the surface effect that appear deeming the perturbation of the turbines virtually negligible.
 359 Near top tip, the flow shows a turbulence of axisymmetric state (between the pancake-like
 360 and cigar-like turbulence). With this representation, the spacing variation leads to a changed
 361 state of the turbulence and between the developed and developing flow conditions can be
 362 discernible. The upstream of case $C_{3 \times 3}$ shows a pancake-like turbulence state. However,
 363 the hub height and bottom tip regions shows an isotropic and axisymmetric turbulence,

364 respectively. The upstream of case $C_{3 \times 1.5}$ exhibits axisymmetric and cigar-like turbulence
365 in the most of the upstream domain, although the hub height region remains described by
366 isotropic turbulence.

367 Past the turbine, the four cases exhibit the turbulence of isotropic state in the hub height
368 region. The top tip region of the four cases shows axisymmetric turbulence although case
369 $C_{3 \times 3}$ tends to be a cigar-like turbulence. Below the hub height, the turbulence is pancake-
370 like and the difference amongst the cases is the covered area, where it is maximum at $C_{6 \times 3}$
371 and minimum at $C_{3 \times 3}$. The longest extension is found in case $C_{6 \times 3}$ and the lowest in case
372 $C_{3 \times 3}$ with. Comparing to $C_{6 \times 3}$, the change seen in the turbulence states is starker in $C_{3 \times 3}$
373 than in $C_{6 \times 1.5}$, confirming that the impact of reducing streamwise spacing is greater than
374 changing the spanwise spacing. However, the impact of the spanwise spacing is noticeable
375 when S_x equals $3D$.

376 The ability to identify the turbulence structure allows for identification of its influence
377 on subsequent turbines in terms of fatigue loads (Frandsen and Thøgersen 1999). Further,
378 regions of the flow that are characterized by highly anisotropic turbulence are those in which
379 one is likely to find large-scale, coherent turbulence structures. These structures impart
380 the greatest axial and bending loads onto subsequent turbine rotors leading to accelerated
381 fatigue and increased operational and maintenance costs for wind farms. In addition, regions
382 of high anisotropy correlate with gradients in the mean flow and turbulence (Hamilton and
383 Cal 2015). These quantities are of particular interest in wind farm modeling and design.
384 Accordingly, the accurate representation of gradients in wind farm design modeling is a
385 necessary check to accurately representing production of and flux by turbulence kinetic
386 energy, wake interaction, and structural loading on constituent turbines. Finally, the stress
387 tensor invariants, by definition, do not depend on reflection or rotation of the coordinate
388 system meaning that they are unbiased descriptive for the turbulent flow (Pope 2000).

389 V. POWER MEASUREMENTS.

390 Figure 14 demonstrates the power produced by each turbine, \mathcal{F}_x , obtained with the torque
391 sensing system, versus the angular velocity, ω . The power measurements are normalized by
392 the maximum theoretical power $\frac{1}{2}\rho A_c U_\infty^3$, where ρ is the air density, A_c is swept area of
393 the turbine rotor $\pi D^2/4$. The angular velocity is normalized by the $2U_\infty/D$. It is apparent

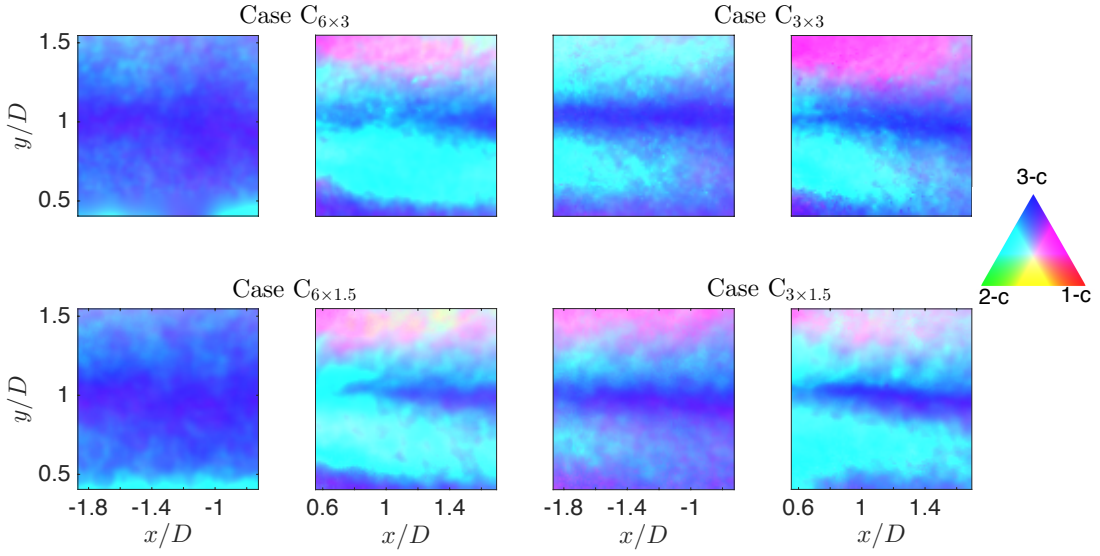


FIG. 13: Barycentric map map for the upstream and downstream of the considered cases. The small triangle is a color map key for ease of interpretation.

394 from the figure that the maximum power is extracted at the normalized angular velocity of
 395 15.8 ± 1 . The maximum normalized power of 0.062 is harvested at the largest spacing, *i.e.*,
 396 case $C_{6 \times 3}$. Fixing the spanwise spacing and decreasing the streamwise spacing reduces the
 397 normalized power produced by 33% for $S_x = 6D$ (from case $C_{6 \times 3}$ to case $C_{3 \times 3}$) and by 22
 398 % for $S_x = 3D$ (from case $C_{3 \times 1.5}$ to case $C_{6 \times 1.5}$). The complementary change in spacing
 399 holds the streamwise spacing constant while decreasing the spanwise spacing. In that case
 400 the normalized power produced is reduced by 20% for $S_z = 3D$ (from case $C_{6 \times 3}$ to case
 401 $C_{6 \times 1.5}$) and by 6% for $S_z = 1.5D$ (from case $C_{3 \times 3}$ to case $C_{3 \times 1.5}$). Nilsson et al. (2015) has
 402 complementary results to the ones present, where an increase in power produced is attained
 403 in the largest spacing and conversely, decreased in the limited spacing case. Furthermore,
 404 increasing the spanwise distance has a less notable effect in comparison to the streamwise
 405 spacing.

406 The trend of the power curves follows the one observed in the averaged profiles of the
 407 streamwise velocity, see figure 7 (a). Further, they verify the relationship between the power
 408 of the turbine with the deficit velocity. The maximum power and velocity are found in the
 409 case $C_{6 \times 3}$ and the minimum quantities are noticed in $C_{3 \times 1.5}$. The smallest variations in the
 410 power measurement and main velocity are observed between cases $C_{3 \times 3}$ and $C_{3 \times 1.5}$, whereas
 411 the largest difference is observed between cases $C_{6 \times 3}$ and $C_{3 \times 3}$. Increased longitudinal
 412 spacing produces larger energy content in the first few modes as to provide the imprint

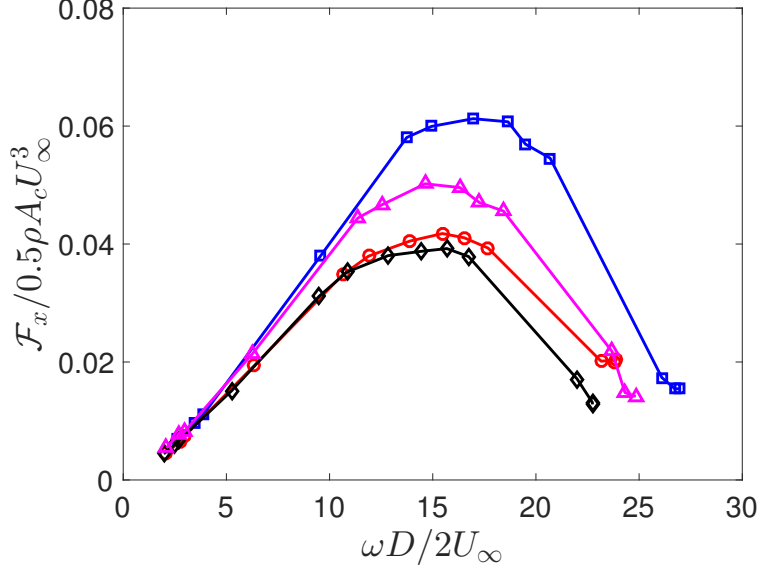


FIG. 14: Extracted power of the wind turbine at different angular velocities for four different cases $C_{6 \times 3}$ (□), $C_{3 \times 3}$ (○), $C_{3 \times 1.5}$ (◇), and $C_{6 \times 1.5}$ (△).

413 of the flow; thus, this is reflected in an increase in power as directly measured via a torque
 414 sensing device.

415 VI. CONCLUSIONS

416 Insight into the behavior of the flow in a wind turbine array is useful in determining how
 417 to highlight the overall power extraction with the variation in spacing between the turbines.
 418 The work above quantifies effects of tightly spaced wind turbine configurations on the flow
 419 behavior. The findings of this study have a number of important implications, especially
 420 regarding the cost of a wind farm or when large areas are not available. Stereographic
 421 PIV data are used to assess characteristic quantities of the flow field in a wind turbine
 422 array with varied streamwise and spanwise spacing. Four cases of different streamwise and
 423 spanwise spacings are examined; the streamwise spacing being $6D$ and $3D$, and spanwise
 424 spacing being $3D$ and $1.5D$. The flow fields are analyzed and compared statistically and by
 425 snapshot proper orthogonal decomposition.

426 The streamwise mean velocity, and Reynolds shear stress are quantified upstream and
 427 downstream of the wind turbine in the considered cases. In the inflow measurement window,
 428 higher velocities are observed in cases $C_{6 \times 3}$ and $C_{6 \times 1.5}$ comparing to the other two cases

429 whose inflows are unrecovered wakes from preceding rows. In contrast, case $C_{3 \times 3}$ and $C_{3 \times 1.5}$
 430 show higher Reynolds shear stress. The notable differences between the cases are found
 431 above the top tip and below the bottom tip downstream the turbines, whereas the core
 432 of the wakes shows fewer discrepancies. The streamwise and spanwise spacings have a
 433 concerted effect on the flow, where the degree of the impact of one change highly depends
 434 on the other. This relationship is shown in all statistical quantities discussed here, such as
 435 reducing of the streamwise spacing by 50% leads to increases in the averaged Reynolds shear
 436 stress by 16% when $S_z = 3D$. According to current statistical quantities, one can infer that
 437 the higher influence of streamwise spacing is shown when the spanwise spacing is $S_z = 3D$,
 438 and the significant effect of the spanwise spacing is observed when the streamwise spacing is
 439 $S_x = 3D$. To make comparisons independent of the effects streamwise spacing, streamwise
 440 average profiles of the statistical quantities are computed. Averaged profiles of the velocity
 441 follow the order of higher velocity seen in the contour plots in case $C_{6 \times 3}$ and lowest velocity
 442 in case $C_{3 \times 1.5}$. The maximum and minimum difference are observed between cases $C_{6 \times 3}$ with
 443 case $C_{3 \times 1.5}$ and $C_{3 \times 3}$ with case $C_{3 \times 1.5}$. The result also reveals that the streamwise spacing
 444 is more impactful than the spanwise spacing. Spatially-averaged profile of Reynolds shear
 445 stress shows the maximum and minimum values occur in cases $C_{3 \times 3}$ and $C_{6 \times 1.5}$, respectively.

446 Based on the POD analysis, the upstream measurement plane of the four cases converges
 447 faster than the downstream window. Case $C_{6 \times 3}$ and $C_{6 \times 1.5}$ show the rapid convergence in
 448 cumulative energy content upstream of the turbine, but $C_{6 \times 3}$ remains behind case $C_{6 \times 1.5}$ in
 449 the wake. The first mode of the case $C_{6 \times 1.5}$ carries the maximum turbulent kinetic energy
 450 content compared to the first mode of the other cases. No significant difference in energy
 451 content is observed after mode 10 between the four cases. The streamwise-averaged profiles
 452 of the Reynolds shear stress are reconstructed by back-projecting coefficients onto the set of
 453 eigenfunctions. Low modes are used individually to demonstrate their contributions to the
 454 overall flow. Cases $C_{6 \times 1.5}$ and $C_{6 \times 3}$ converge to the total spatially-averaged profile faster
 455 than other two cases and the discrepancy in reconstruction is mainly observed in profiles
 456 using only the first five modes. The same trend in reconstruction is observed in cases $C_{3 \times 3}$
 457 and $C_{3 \times 1.5}$. Reconstructed profiles display the effects of the spacing, where the array of large
 458 streamwise spacing reconstruct faster than the other cases due to the coherent structures
 459 embedded within the flow.

460 Based on the anisotropy stress tensor and color map visualization, the spacing modifies

461 the turbulence structure and the longest spacing attenuates the perturbation of the turbu-
462 lence, inducing the flow towards a more isotropic state. The hub height region shows an
463 isotropic turbulence state regardless the spacing. The differences of the color map visualiza-
464 tion between the downstream locations of the four cases show some structural dependency
465 on the spacing between turbine rotors.

466 Power production by the turbines is measured directly using torque sensing system. The
467 power curves follow the same trend as the velocity profiles. The maximum power extracted
468 at the normalized angular velocity of 15.8 ± 1 and it is harvested in case $C_{6 \times 3}$. The small
469 difference in harvested power is observed between cases $C_{3 \times 3}$ and $C_{3 \times 1.5}$. The current work
470 demonstrates that wake statistics and power produced by a wind turbine depend more on
471 streamwise spacing than spanwise spacing. However, results above pertain only to a fixed
472 inflow direction. In the case where the bulk flow orientation changes, spacing in both the
473 streamwise and spanwise directions will be important to the optimal power production in
474 a wind turbine array. Continued efforts are required to understand the impact of stream-
475 wise and spanwise spacing in infinite array flow with Coriolis forcing and under different
476 stratification conditions.

477 Acknowledgments

478 Naseem Ali acknowledges support from the Higher Committee of Education Development
479 in Iraq (HCED). The authors are grateful to NSF-ECCS-1032647 for funding this research.

480 B. Viggiano, M. S. Gion, N. Ali, M. Tutkun, and R. B. Cal, *Journal of Renewable and Sustainable*
481 *Energy* **8**, 053310 (2016).

482 N. Ali, A. S. Aseyev, and R. B. Cal, *Journal of Renewable and Sustainable Energy* **8**, 013304
483 (2016a).

484 R. J. Barthelmie, S. T. Frandsen, M. N. Nielsen, S. C. Pryor, P.-E. Rethore, and H. E. Jørgensen,
485 *Wind Energy* **10**, 517 (2007).

486 L. P. Chamorro and F. Porté-Agel, *Boundary-layer meteorology* **132**, 129 (2009).

487 L. P. Chamorro and F. Porté-Agel, *Energies* **4**, 1916 (2011).

488 R. J. Barthelmie, S. C. Pryor, S. T. Frandsen, K. S. Hansen, J. G. Schepers, K. Rados, W. Schlez,
489 A. Neubert, L. E. Jensen, and S. Neckelmann, *Journal of Atmospheric and Oceanic Technology*
490 **27**, 1302 (2010).

491 R. J. Barthelmie and L. E. Jensen, *Wind Energy* **13**, 573 (2010).

492 K. S. Hansen, R. J. Barthelmie, L. E. Jensen, and A. Sommer, *Wind Energy* **15**, 183 (2012).

493 F. González-Longatt, P. Wall, and V. Terzija, *Renewable Energy* **39**, 329 (2012).

494 J. Meyers and C. Meneveau, *Wind Energy* **15**, 305 (2012).

495 R. J. Stevens, *Wind Energy* p. 10.1002/we.1857 (2015).

496 D. Romanic, D. Parvu, M. Refan, and H. Hangan, *Renewable Energy* **115**, 97 (2018).

497 K. Nilsson, S. Ivanell, K. S. Hansen, R. Mikkelsen, J. N. Sørensen, S.-P. Breton, and D. Henningson,
498 *Wind Energy* **18**, 449 (2015).

499 J. Meyers and C. Meneveau, *AIAA* **827**, 2010 (2010).

500 X. Yang, S. Kang, and F. Sotiropoulos, *Physics of Fluids (1994-present)* **24**, 115107 (2012).

501 Y.-T. Wu and F. Porté-Agel, *Boundary-Layer Meteorology* **146**, 181 (2013).

502 C. L. Archer, S. Mirzaeisefat, and S. Lee, *Geophysical Research Letters* **40**, 4963 (2013).

503 R. J. Stevens, D. F. Gayme, and C. Meneveau, *Wind Energy* **19**, 359 (2016).

504 J. L. Lumley, *Atmospheric Turbulence and Radio Wave Propagation* pp. 166–178 (1967).

505 L. Sirovich, *Quarterly of Applied Mathematics* **45**, 561 (1987).

506 M. N. Glauser and W. K. George, in *Advances in Turbulence* (Springer, 1987), pp. 357–366.

507 P. Moin and R. D. Moser, *Journal of Fluid Mechanics* **200**, 471 (1989).

508 S. Shah and E. Bou-Zeid, *Boundary-Layer Meteorology* **153**, 355 (2014).

509 M. Tutkun, P. B. Johansson, and W. K. George, *AIAA* **46**, 1118 (2008).

510 S. J. Andersen, J. N. Sørensen, and R. Mikkelsen, *Journal of Turbulence* **14**, 1 (2013).

511 D. Bastine, B. Witha, M. Wächter, and J. Peinke, *Journal of Physics: Conference Series* **524**,
512 012153 (2014).

513 C. VerHulst and C. Meneveau, *Physics of Fluids* **26**, 025113 (2014).

514 N. Hamilton, M. Tutkun, and R. B. Cal, *Wind Energy* **18**, 297 (2015a).

515 N. Ali, H. F. Kadum, and R. B. Cal, *Journal of Renewable and Sustainable Energy* **8**, 063306
516 (2016b).

517 N. Ali, G. Cortina, N. Hamilton, M. Calaf, and R. B. Cal, *Journal of Fluid Mechanics* **828**, 175
518 (2017a).

519 J. Rotta, *Z. Physik* **131** (1951).

520 S. B. Pope, *Turbulent flows* (Cambridge University Press, 2000).

521 J. L. Lumley and G. R. Newman, *Journal of Fluid Mechanics*. **82**, 161 (1977).

522 S. Banerjee, R. Krahl, F. Durst, and C. Zenger, *Journal of Turbulence* **8**, N32 (2007).

523 M. Emory and G. Iaccarino, Annual Brief, Center for Turbulence Research (2014).

524 R. A. Antonia, J. Kim, and L. Browne, *Journal of Fluid Mechanics*. **233**, 369 (1991).

525 P. Krogstad and L. E. Torbergsen, *Flow, turbulence and combustion*. **64**, 161 (2000).

526 C. Klipp, in *SPIE Defense, Security, and Sensing*. (International Society for Optics and Photonics.,
527 2010), pp. 768505–768505.

528 C. Klipp, in *SPIE Defense, Security, and Sensing*. (International Society for Optics and Photonics.,
529 2012), p. 83800G.

530 R. Gómez-Elvira, A. Crespo, E. Migoya, F. Manuel, and J. Hernández, *Journal of Wind Engineering*
531 *and Industrial Aerodynamics*. **93**, 797 (2005).

532 N. Hamilton and R. B. Cal, *Physics of Fluids*. **27**, 015102 (2015).

533 N. Ali, A. S. Aseyev, M. S. Melius, M. Tutkun, and R. B. Cal, in *Whither Turbulence and Big*
534 *Data in the 21st Century?* (Springer, 2017b), pp. 273–292.

535 N. Ali, N. Hamilton, G. Cortina, M. Calaf, and R. B. Cal, *Journal of Renewable and Sustainable*
536 *Energy* **9** (2017c).

537 L. P. Chamorro, R. Arndt, and F. Sotiropoulos, *Wind Energy* **15**, 733 (2012).

538 R. B. Cal, J. Lebrón, L. Castillo, H. S. Kang, and C. Meneveau, *Journal of Renewable and*
539 *Sustainable Energy* **2**, 013106 (2010).

540 H. S. Kang and C. Meneveau, *Measurement Science and Technology* **21**, 105206 (2010).

541 N. Hamilton, M. Melius, and R. B. Cal, *Wind Energy* **18**, 277 (2015b).

542 W. K. George, Chalmers University of Technology (2013).

543 S. Frandsen and M. L. Thøgersen, *Wind Engineering* pp. 327–339 (1999).